EFFECTS OF STRONG TEMPERATURE GRADIENT ON A COMPRESSIBLE TURBULENT CHANNEL FLOW

Mitsuhiro Nagata

Mechanical Engineering Dept. I
TOYOTA Central R&D Labs., Inc.
41-1, Yokomichi, Nagakute, Aichi 480-1192, Japan
nagata@mosk.tytlabs.co.jp

Makoto Nagaoka

Mechanical Engineering Dept. I
TOYOTA Central R&D Labs., Inc.
41-1, Yokomichi, Nagakute, Aichi 480-1192, Japan
nagaoka@mosk.tytlabs.co.jp

ABSTRACT

A direct numerical simulation of a compressible turbulent channel flow at low-Mach number (Ma = 0.3) subject to a strong temperature gradient is conducted. The wall temperature ratios, which are defined by the temperature on the upper wall divided by that on the lower wall, are set to 2 and 3. It is shown that the flow on the high-temperature side is laminarized as the wall temperature ratio increases. Moreover, compressible and dilatational motions are induced on the low- and high-temperature wall sides, respectively. The identity equation of the friction coefficient originally derived by Fukagata et al. (2002) is extended to those of the friction coefficient and Nusselt number in a compressible channel flow. The viscous variation component is shown to reach 16% of the friction coefficient in the case of a high temperature ratio. Furthermore, the pressure work component occupies approximately 20% of the overall Nusselt number for all cases. The pressure work has a redistributive effect between mean kinetic and internal energies. The energy transfer on the low-temperature side is from the mean kinetic energy to the internal energy, whereas the energy transfer on the high-temperature side is from the internal energy to the mean kinetic energy, even in the present low-Mach number flow.

INTRODUCTION

High-temperature wall turbulence commonly appears in combustion chambers with cooling system and so forth. In order to achieve high-efficiency industrial instruments, it is important to clarify this phenomenon.

Numerical simulation of a compressible turbulent channel flow with a high-temperature gradient induced by a temperature difference between two walls has been performed by relatively few researchers. Wang and Pletcher (1996) examined this problem with a preconditioning method in order to avoid encountering the stiffness problem in a low-Mach number flow. In their calculation, the spatial Favre-filtered variables are obtained because a dynamic subgrid-scale model is adopted. Moreover, pressure and viscous works, which are intrinsic features of the compressible flow, are neglected. Nicoud (2000) also simulated this problem under the low-Mach number assumption. His research was devoted primarily to the proposal of an energy conservative scheme under the low-Mach number assumption, therefore few computational results were presented. Tamano and Morinishi (2006) simulated a fully compressible turbulent channel flow with a high temperature gradient at Ma = 1.5 using a high-accuracy spectral method. Their result revealed that the region in which the mean temperature exceeded the high wall temperature appeared as a result of the viscous work of the high-speed flow.

To the best of our knowledge, in the previous studies, the DNS of the low-Mach number turbulent channel flow with a high temperature gradient, in which the pressure and viscous works were taken into account, was not seen.

In the present study, the DNS of a fully compressible turbulent channel flow with a high temperature gradient at low-Mach number is investigated in order to reveal the momentum and heat transfer mechanisms. Furthermore, the identity equation of the friction coefficient originally derived by Fukagata et al. (2002) is extended to the friction coefficient and Nusselt number in a compressible channel flow in order to clarify which component is dominant in the wall friction or heat transfer at the wall.

COMPUTATIONAL CONFIGURATION AND NUMERICAL METHODOLOGY

Figure 1 shows the computational domain, in which x, y, and z (or x_1, x_2, and x_3) represent the streamwise, wall-normal, and spanwise coordinates, respectively, and the velocity components are u, v, and w (or u_1, u_2, and u_3) in a similar order. The temperature at the upper wall is represented by T_H, and that at the lower wall is represented by T_L. The computational conditions are listed in Table 1. Hereinafter, terms with superscripts H and L represent values at the high- and low-temperature walls, respectively. Table 2 shows the non-dimensional parameters. The Reynolds number Re is defined by the bulk velocity U_b, the channel half width h, the bulk density ρ_b, and the viscosity at the

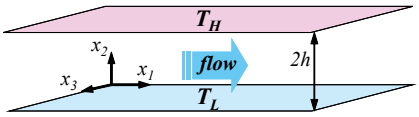

Figure 1. Computational domain.

Table 1. Computational conditions.

	Case1	Case2
T_L(K)	293	293
T_H(K)	586	879
T_H/T_L	2	3

Table 2. Non-dimensional parameters.

Re	2,220
Pr	0.71
Ma	0.3
γ	1.4

lower wall μ_L. The Mach number is defined as $Ma = U_b/\sqrt{\gamma R T_L}$, where γ is the specific heat ratio, and R is the gas constant. The working fluid is assumed as air, and the temperature dependency of viscosity is expressed by the Sutherland law. The variables are non-dimensionalized by the values used for the definition of the non-dimensional parameters, unless otherwise stated. On the other hand, values with superscript + represent values that are non-dimensionalized by wall-variables. Flow is driven by a constant mass flow rate condition. The periodic boundary conditions in the two homogeneous directions (x and z) are applied, whereas non-slip boundary conditions are applied at the two walls. The computational domain is $2.5\pi h \times 2h \times \pi h$ (in the x, y, and z directions) with 96×128×96 grid points. Fully compressible Navier-Stokes equations are discretized by the sixth-order compact finite difference scheme (Lele, 1992) in the x and z directions. For the y direction, a second-order central finite difference scheme is applied. No numerical diffusion scheme, such as upwinding or spatial filtering, is used because numerical stability is ensured by adopting a staggered grid system (Nagarajan et al., 2003). Time integration is performed by the Wray-type third-order Runge-Kutta scheme. The computation is conducted at least for $600h/U_b$. After confirming that the flow reaches a statistically steady state, the computation continues for $300h/U_b$ in order to collect the statistical quantities.

INSTANTANEOUS FLOW STRUCTURES

Figure 2 shows the vortical structures and temperature distribution. The second invariant of the velocity gradient tensor is adopted as an indicator of the vortical structures:

$$II = \frac{1}{2}\left(\left(\frac{\partial u_k}{\partial x_k}\right)^2 - \frac{\partial u_i}{\partial x_j}\frac{\partial u_j}{\partial x_i}\right) \quad (1)$$

The value of the second invariant is set to $IIh^2/U_b^2 = 1$ throughout the visualizations. In the case of $T_H/T_L = 2$ (Fig. 2(a)), vortical structures are tilted toward the wall and are coherently distributed on the low-temperature side. This distribution is significantly similar to that in the incompressible case. On the other hand, vortex motion is significantly suppressed on the high-temperature side. As the temperature ratio T_H/T_L increases, the vortical structure disappears on the high-temperature side (Fig. 2(b)). Figs. 3 and 4 show top-down views of vortical structures and wall heat flux. On the low-temperature side (Figs. 3(a) and 4(a)), vortical structures coincide with high wall heat flux regions, as shown in the incompressible flow with the passive scalar. On the other hand, vortical structures are scarcely seen and high/low heat flux regions are elongated almost linearly on the high-temperature side. These features are attributed to the laminarizing effect over the high-temperature wall as a result of a decrease in density (shown later) and an increase in viscosity.

TURBULENCE STATISTICS

The friction coefficient and Nusselt number are defined as follows:

$$C_f = \frac{\tau_w}{\frac{1}{2}\rho_b U_b^2} \quad (2)$$

$$Nu = \frac{2\alpha y_b}{\lambda} = \frac{2y_b \left.\frac{\partial T}{\partial y}\right|_w}{T_b - T_w} \quad (3)$$

where τ_w, λ, and α are the wall shear stress, the thermal conductivity, and the heat transfer rate, respectively, T_b is the bulk temperature, and y_b corresponds to the wall-normal position, where the mean temperature is equal to T_b. Figure 5 shows the temperature ratio dependency of C_f and Nu. Each value is normalized by the incompressible/passive scalar value (C_{fi} or Nu_i in Fig. 5) evaluated by Kasagi and Iida (1999). Moreover, C_f gradually becomes larger as the temperature ratio increases. On the other hand, Nu decreases significantly, whereas C_f is approximately constant on the high-temperature wall. This is due primarily to the decrease in the temperature gradient at the wall as a result of the laminarizing effect, as shown in Fig. 2.

The first invariant of the mean velocity gradient tensor is expressed as

$$I = \frac{\partial \overline{u}_k}{\partial x_k} \quad (4)$$

The value of I is less than 0 for compressible motion, is greater than 0 for dilatational motion, and is equal to 0 for an incompressible flow. The first invariant distribution is shown in Fig. 6. The compressible and dilatational motions are induced over the low- and high-temperature walls, respectively. The enhancement of the absolute value of I is seen as increasing the temperature ratio. Therefore, more strong compressible /dilatational motions appear. As a consequence of these motions, the mean vertical velocity from the high-temperature wall to the low-temperature wall is induced, as shown in Fig. 7. Moreover, an increased vertical velocity is seen as increasing the temperature ratio.

Figure 8 represents the mean temperature distribution. The symbols indicate the results reported by Na et al. (1999) for the turbulent flow with a passive scalar, and each result is rescaled to correspond with the present case. Although the difference between the present result and the result reported by Na et al. (1999) is limited in the region near the high-temperature wall in the case of $T_H/T_L = 2$, a large region in which the temperature

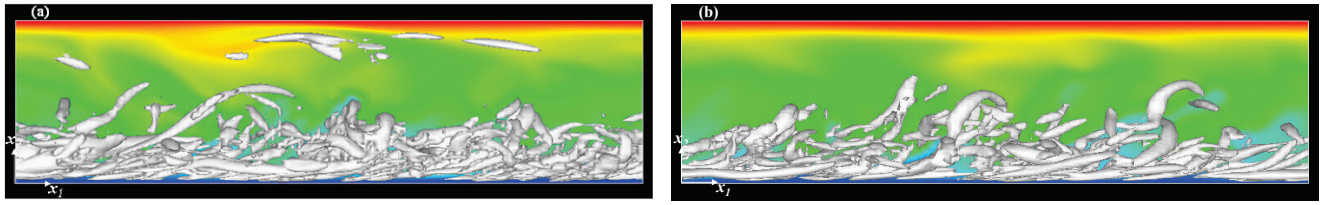

Figure 2. Instantaneous flow structures: side view, (a) $T_H/T_L = 2$; (b) $T_H/T_L = 3$. White, vortical structure; color contour, temperature distribution which ranges from blue ($T = T_L$) to red ($T = T_H$).

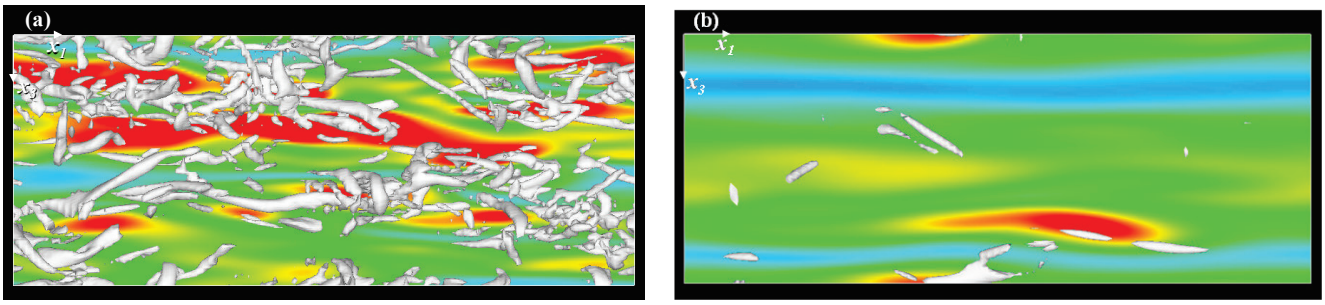

Figure 3. Instantaneous flow structures at $T_H/T_L = 2$: top view, (a) low temperature side; (b) high temperature side. White, vortical structure; color contour, wall heat flux with high value ($q_w = 5$) represented by red and low one ($q_w = 0$) by blue.

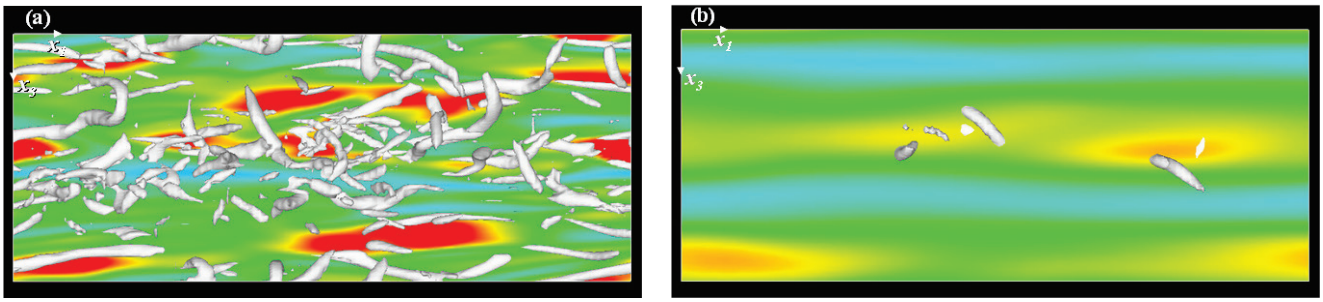

Figure 4. Instantaneous flow structures at $T_H/T_L = 3$: top view, (a) low temperature side; (b) high temperature side. White, vortical structure; color contour, wall heat flux with high value ($q_w = 10$) represented by red and low one ($q_w = 0$) by blue.

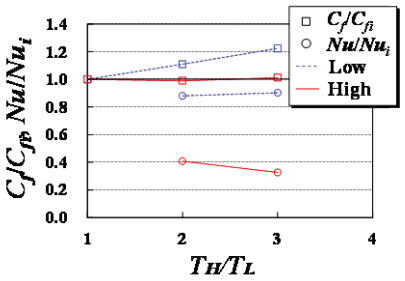

Figure 5. Friction coefficient and Nusselt number.

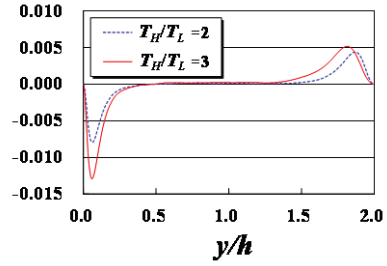

Figure 6. First invariant distribution.

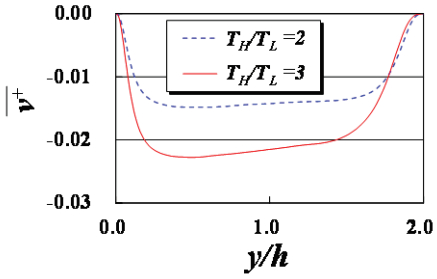

Figure 7. Vertical velocity profiles.

distribution is lower than that of the passive scalar case is observed at $T_H/T_L = 3$. In addition, the temperature gradient at the high-temperature wall is considerably decreased. Since pressure is approximately constant across the channel in the present cases, the density is inversely proportional to the temperature. As shown in Fig. 9, the mean density takes the lowest value on the high-temperature wall and gradually varies on that side. This density distribution affects the value of C_f as described in the later section.

Turbulence intensities are shown in Fig. 10 with the incompressible channel database reported by Iwamoto et al. (2002) referred to as '*ISK*' in the figure. The peak of *u'* on the high-temperature wall side moves toward the center of the channel as the temperature ratio increases and both *v'* and *w'* are extensively weakened. These characteristics are common features when the flow becomes laminarized. On the other hand, the turbulence intensities on the low-temperature wall side are similar for all cases and correspond well to those for the incompressible flow.

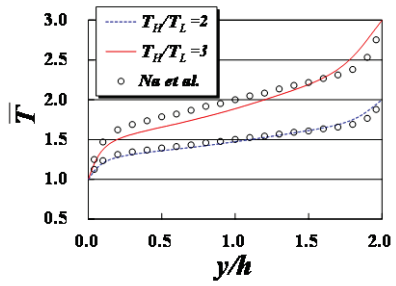

Figure 8. Mean temperature distribution.

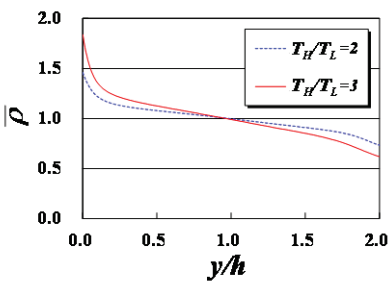

Figure 9. Mean density profiles.

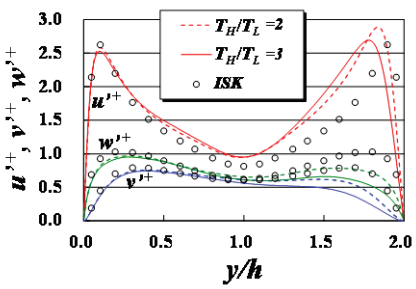

Figure 10. Turbulence intensities.

COMPONENTIAL DECOMPOSITION OF THE FRICTION COEFFICIENT

Fukagata et al. (2002) derived the identity equation of C_f on the incompressible wall turbulence, which is described by the linear combination of laminar and turbulent components ('*FIK identity*'). In the present study, this identity is extended to those of C_f and Nu on the compressible turbulent channel flow, and, according to these identities, each component of C_f and Nu is quantified.

Identity Equation of the Friction Coefficient in a Compressible Channel Flow

By triple integration normal to the wall of the mean streamwise momentum equation, we obtain the following identity of C_f for the compressible channel flow:

$$C_{fa} = \frac{3\mu_L}{\mathrm{Re}}\int_0^2 \overline{u}\,dy + 3\int_0^2 (1-y)\left(-\overline{\rho}\{u''v''\}\right)dy + \frac{3}{\mathrm{Re}}\int_0^2 (1-y)(V+V')dy \qquad (5)$$

where { } and ( )" represent the Favre average and the fluctuation from the Favre averaged value, respectively, and V and V' are the mean and fluctuation components, respectively, of the viscous variance:

$$V = (\overline{\mu} - \mu_L)\frac{\partial \overline{u}}{\partial y} \qquad (6a)$$

$$V' = \overline{\mu' \frac{\partial u'}{\partial y}} + \overline{\mu' \frac{\partial v'}{\partial x}} \qquad (6b)$$

In eq. (5), C_{fa} is the overall friction coefficient, which is defined by

$$C_{fa} = \frac{(\tau_{wL} + \tau_{wH})/2}{\frac{1}{2}\rho_b U_b^2} = \frac{C_{fL} + C_{fH}}{2} \qquad (7)$$

Table 3. Friction coefficients.

	$C_{fa}\times 10^3$	
	$T_H/T_L = 2$	$T_H/T_L = 3$
Evaluated by eq. (5)	9.12	9.71
Directly computed	9.09	9.67

Note that each C_{fL} or C_{fH} previously shown in Fig. 5 is not able to be decomposed into components as C_{fa} decomposition (eq. (5)). The friction coefficients are presented in Table 3. It is confirmed that C_{fa} evaluated by eq. (5) preferably coincides with the directly computed value obtained by eq. (7). The laminar, turbulence, and viscous variance components correspond to the first, second, and last terms in eq. (5), respectively.

Evaluation of Friction Coefficient Components

The results of C_{fa} decomposition are shown in Fig. 11 along with the results for an incompressible flow reported by Fukagata et al. (2002). The laminar component has a similar value for all cases. Moreover, the turbulence component also varies only slightly for two temperature ratios. This feature is due primarily to the increase in mean density on the low-temperature side (shown in Fig. 9), by which the turbulent shear stress is multiplied in the turbulence component (as seen in the second term of eq. (5)), whereas the turbulent motion is significantly suppressed on the high-temperature wall side as the temperature ratio increases (see Fig. 10). On the other hand, the viscous variance component is enhanced as the temperature ratio increases. Fig. 12 shows the fraction of C_{fa} components. Each component is normalized by the overall value of C_{fa}. Although the turbulence component decreases as the temperature ratio increases, this is a virtual appearance owing to the overall increase in C_{fa}. The viscous variance component reaches

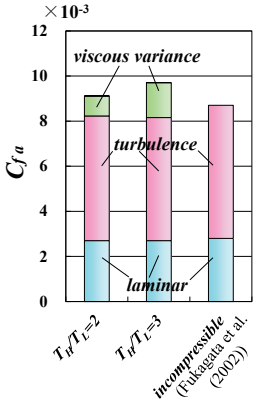

Figure 11. Componential decomposition of C_{fa}.

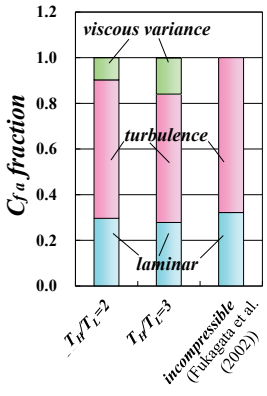

Figure 12. Fraction of C_{fa} components.

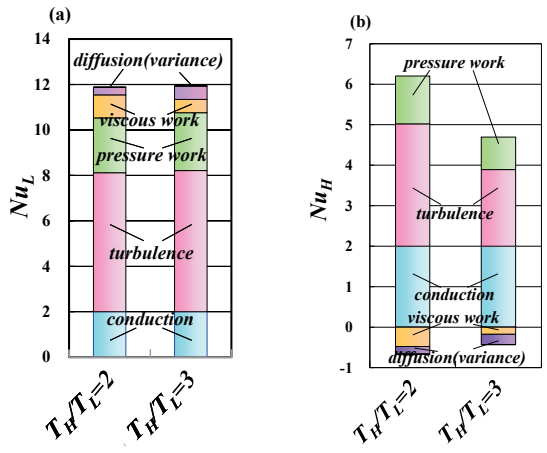

Figure 13. Componential decomposition of *Nu*: (a) Nu_L; (b) Nu_H.

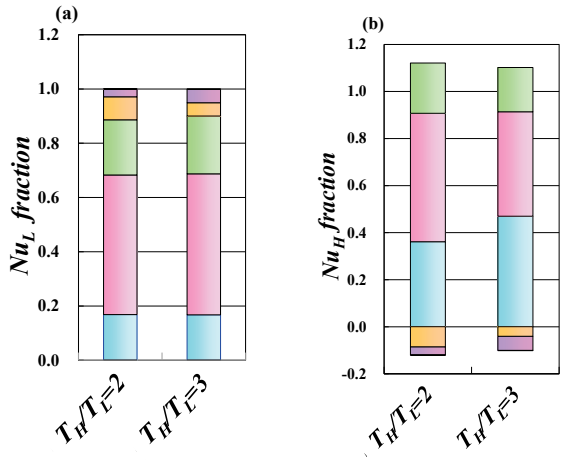

Figure 14. Fraction of *Nu* components: (a) Nu_L; (b) Nu_H. Colors as in Figure 13.

approximately 10% and 16% of C_{fa} for T_H/T_L = 2 and 3, respectively.

DECOMPOSITION OF THE NUSSELT NUMBER

A similar procedure for C_{fa} decomposition as described in the previous section is also applicable to the Nusselt number. In this section, the identity of the Nusselt number is derived, and each component is evaluated precisely.

Identity of the Nusselt Number on the Compressible Channel Flow

The identity of the Nusselt number is obtained through double integration normal to the wall of the mean internal energy equation.

$$Nu = 2 + \frac{2\,\mathrm{Re}\,\mathrm{Pr}}{\gamma\lambda_0(T_b - \overline{T}|_{y=0})}\int_0^{y_b}(-\overline{\rho}\{v''T''\})dy - \frac{2\,\mathrm{Re}\,\mathrm{Pr}}{\gamma\lambda_0(T_b - \overline{T}|_{y=0})}\int_0^{y_b}(y_b - y)P_w dy + \frac{2\,\mathrm{Re}\,\mathrm{Pr}}{\gamma\lambda_0(T_b - \overline{T}|_{y=0})}\int_0^{y_b}(y_b - y)V_w dy + \frac{2}{\lambda_0(T_b - \overline{T}|_{y=0})}\int_0^{y_b} D dy \quad (8)$$

where P_w, V_w, and D are the constitutions of the pressure work, viscous work, and diffusion coefficient variance, respectively, given by

$$P_w = (\gamma - 1)\overline{\rho T\frac{\partial u_i}{\partial x_i}} \quad (9a)$$

$$V_w = \frac{Ma^2}{\mathrm{Re}}\gamma(\gamma - 1)\overline{\sigma_{ij}\frac{\partial u_i}{\partial x_j}} \quad (9b)$$

$$D = \overline{(\lambda - \lambda_0)\frac{\partial T}{\partial y}} \quad (9c)$$

in which λ_0 is the thermal conductivity at the wall, and σ_{ij} is a viscous stress tensor. Good agreement between the values of *Nu* evaluated through the identity (eq. (8)) and those computed directly is confirmed (not shown here). The first, second, third, fourth, and last terms on the right-hand side of eq. (8) correspond to the conduction (value of 2), turbulence, pressure work, viscous work, and diffusion (variance), respectively. The third through last terms in eq. (8) vanish for the incompressible/passive scalar flow.

Evaluation of the Nusselt Number Components

Fig. 13 shows the componential decomposition of *Nu*. The turbulence component takes a similar value to Nu_L between the cases of T_H/T_L = 2 and 3. On the other hand, the turbulence component decreases noticeably as the temperature ratio increases on the high-temperature wall, as shown in Fig. 13(b). This tendency is consistent with the attenuation of turbulence intensities shown in Fig. 10. The pressure work component has a large positive contribution to both of Nu_L and Nu_H. The viscous work and diffusion components are not negligible on *Nu* and have a negative contribution on the high temperature wall (Fig. 13(b)) because the direction of heat flux, which is away from the wall, is defined as positive on the high-temperature wall. The fraction of *Nu* components is depicted in Fig. 14. It is confirmed that the pressure work component occupies approximately 20% of the overall *Nu* for all cases.

Role of Pressure Work

In the previous section, the pressure work component is observed to occupy approximately 20% of the overall Nusselt number. The role of pressure work is examined in this section.

The mean internal energy budget (for instance, Huang et al. (1995)) is given as follows:

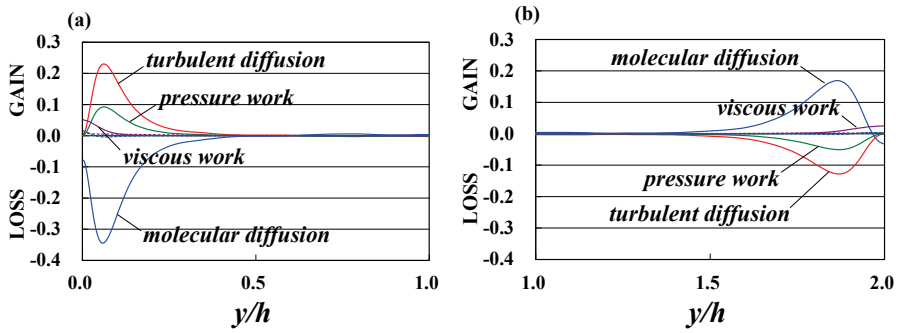

Figure 15. Budgets of internal energy at $T_H/T_L = 2$: (a) low-temperature side; (b) high-temperature side.

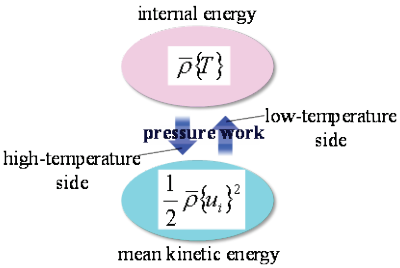

Figure 16. Schematic of energy transfer by the pressure work.

$$\frac{\partial \overline{\rho}\{T\}}{\partial t} = -\frac{\partial}{\partial x_2}\left(\overline{\rho}\{u_2''T''\}\right) - (\gamma-1)\overline{\rho T}\frac{\partial \overline{u}_k}{\partial x_k} - (\gamma-1)\overline{(\rho T)'\frac{\partial u_k'}{\partial x_k}} + \frac{(\gamma-1)\gamma Ma^2}{\mathrm{Re}}\left(\overline{\mu\sigma_{ij}}\frac{\partial \overline{u}_i}{\partial x_j} + \overline{(\mu\sigma_{ij})'\frac{\partial u_i'}{\partial x_j}}\right) + \frac{\gamma}{\mathrm{Re}\,\mathrm{Pr}}\left(\frac{\partial}{\partial x_k}\left(\overline{\lambda}\frac{\partial \overline{T}}{\partial x_k} + \overline{\lambda'\frac{\partial T'}{\partial x_k}}\right)\right) \quad (10)$$

The first term on the right-hand side of eq. (10) is the turbulent diffusion, the second is the pressure work, the third is the pressure-dilatation correlation, the fourth is the viscous work, and the last term is the molecular diffusion. Pressure work exhibits a redistributive effect between the internal and mean kinetic energies because pressure work having the opposite sign to that in eq. (10) also appears in the mean kinetic energy budget. Fig. 15 represents the budgets of internal energy at $T_H/T_L = 2$. On the low-temperature side (Fig. 15(a)), the main source of internal energy is turbulent diffusion, whereas the sink is molecular diffusion. Since the sign of pressure work is positive, the energy flow from mean kinetic to internal energy arises over the low-temperature wall. On the other hand, pressure work has a negative value on the high-temperature wall side (Fig. 15(b)). Therefore, energy flow from internal to mean kinetic energy is induced over the high-temperature wall. These energy flows are depicted schematically in Fig. 16. The pressure work has a major effect on *Nu*, as shown in Fig. 13, through the above-mentioned mechanism.

CONCLUSION

Direct numerical simulation of a compressible turbulent channel flow subject to a strong temperature gradient at low Mach number was performed. An increase in temperature ratio caused the flow to laminarize over the high-temperature wall. Compressible and dilatational motions were induced on the low- and high-temperature wall sides, respectively. Consequently, the mean vertical flow occurs from the high-temperature wall to the low-temperature wall. The identity of the friction coefficient for the compressible channel flow was derived through the procedure proposed by Fukagata et al. (2002). The viscous variance component was enhanced as the temperature ratio increased. The identity of the Nusselt number was also derived. The viscous work and diffusion components were not negligible, and the pressure work was shown to reach approximately 20% of the overall Nusselt number. The energy transfer between the mean kinetic and internal energies through the pressure work was clarified, even in the present low-Mach number flow.

REFERENCES

Fukagata, K., Iwamoto, K., and Kasagi, N., 2002, "Contribution of Reynolds Stress Distribution to the Skin Friction in Wall-Bounded Flows", *Physics of Fluids*, Vol. 14, pp. L73-L76.

Huang, P. G., Coleman, G. N., and Bradshaw, P., 1995, "Compressible Turbulent Channel Flows: DNS Results and Modelling", *Journal of Fluid Mechanics*, Vol. 305, pp. 185-218.

Iwamoto, K., Suzuki, Y., and Kasagi, N., 2002, "Reynolds Number Effect on Wall Turbulence: toward Effective Feedback Control", *International Journal of Heat and Fluid Flow*, Vol. 23, pp. 678-689.

Kasagi, N., and Iida, O., 1999, "Progress in Direct Numerical Simulation of Turbulent Heat Transfer", *Proceedings of the 5th ASME/KSME Joint Thermal Engineering Conference*, ASME, San Diego, Paper No. AJTE99-6302, pp. 1-17.

Lele, S. K., 1992, "Compact Finite-Difference Schemes with Spectral-like Resolution", *Journal of Computational Physics*, Vol. 103, pp. 16-42.

Na, Y., Papavassiliou, D. V., and Hanratty, T. J., 1999, "Use of Direct Numerical Simulation to Study the Effect of Prandtl Number on Temperature Fields", *International Journal of Heat and Fluid Flow*, Vol. 20, pp. 187-195.

Nagarajan, S., Lele, S. K., and Ferziger, J. H., 2003, "A Robust High-Order Compact Method for Large Eddy Simulation", *Journal of Computational Physics*, Vol. 191, pp. 392-419.

Nicoud, F., 2000, "Conservative High-Oder Finite-Difference Schemes for Low-Mach Number Flows", *Journal of Computational Physics*, Vol. 191, pp. 392- 419.

Tamano, S., and Morinishi, Y., 2006, "Effect of Different Thermal Wall Boundary Conditions on Compressible Turbulent Channel Flow at M = 1.5", *Journal of Fluid Mechanics*, Vol. 548, pp. 361- 373.

Wang, W. K., and Pletcher, R. H., 1996, "On the Large Eddy Simulation of a Turbulent Channel Flow with Significant Heat Transfer", *Physics of Fluids*, Vol. 8, pp. 3354-3366.